Effect of Li on the deformation mechanisms of nanocrystalline hexagonal close packed magnesium

Karewar, S.; Gupta, N.; Groh, S.; Martinez, E.; Caro, A.; Srinivasan, S.G.

DOI
10.1016/j.commatsci.2016.09.002

Publication date
2017

Document Version
Accepted author manuscript

Published in
Computational Materials Science

Link to formal publication Computational Materials Science (Elsevier): http://dx.doi.org/10.1016/j.commatsci.2016.09.002

Effect of Li on the deformation mechanisms of nanocrystalline hexagonal close packed Magnesium

S. Karewar[1], N. Gupta[2], S. Groh [3],
E. Martinez [4], A. Caro[4] †, S. G. Srinivasan[2] *
[1] *Department of Materials Science and Engineering, Delft University of Technology, Delft, The Netherlands*;
[2] *Department of Materials Science and Engineering, University of North Texas, Denton, TX*;
[3] *Department of Biomedical Engineering, University of Basel, Basel, Switzerland*;
[4] *Materials Science and Technology Division, Los Alamos National Laboratory, Los Alamos, NM*

Abstract

Addition of solutes such as lithium enhances ductility of hexagonal-close-packed (hcp) Magnesium (Mg). However, the atomistic underpinning of Li addition on individual deformation mechanisms remain unclear and is the focus of the present work. We compared the deformation mechanisms in nanocrystalline (NC) and single crystal simulation systems of pure Mg and Mg-Li hcp alloys. Five deformation modes are observed in the pure NC Mg with randomly oriented grains – one basal $\{0001\}\ \langle 11\bar{2}0\rangle$, one pyramidal type-I $\{10\bar{1}1\}\ \langle 11\bar{2}3\rangle$, and three twinning slip systems $\{10\bar{1}2\}\ \langle 10\bar{1}1\rangle$, $\{10\bar{1}3\}\ \langle 30\bar{3}2\rangle$, and $\{10\bar{1}1\}\ \langle 10\bar{1}2\rangle$. Distributing 10 at.% Li randomly to this NC Mg decreased its compressive yield strength by 14.5%. This also increases the ductility by activating non-basal deformation modes and by reducing the plastic anisotropy. We benchmarked these results by comparing the effect of Li addition on these deformation modes in Mg single crystals. Finally, we present a formability parameter (F_p) model based on unstable stacking fault energy, twin fault energy, and nucleation stress for dislocations (τ_{NS}). Quantifying the changes in F_p values for the Mg-Li alloys with respect to pure Mg in single crystal simulations explain the decrease in compressive yield strength and change in deformation mechanisms with Li additions. A sensitivity analysis study, comparing our CD-EAM results with a MEAM potential, shows that the effects of Li on the single deformation mechanisms are potential independent. Lastly, while results for Mg-10 at.% Li random alloy are presented here, similar conclusions can be drawn for other compositions of this hcp Mg-Li alloy.

Keywords: Nanocrystalline deformations, single crystal, Mg, Mg-Li alloys, plastic anisotropy, dislocation, twins

[1] *Corresponding Author srinivasan.srivilliputhur@unt.edu
[2] †On leave of absence to NSF (jcaro@nsf.gov)

Effect of Li on the deformation mechanisms of nanocrystalline hexagonal close packed Magnesium

S. Karewar[1], N. Gupta[2], S. Groh [3],
E. Martinez [4], A. Caro[4] †, S. G. Srinivasan[2] *
[1]*Department of Materials Science and Engineering, Delft University of Technology, Delft, The Netherlands*;
[2]*Department of Materials Science and Engineering, University of North Texas, Denton, TX*;
[3]*Department of Biomedical Engineering, University of Basel, Basel, Switzerland*;
[4]*Materials Science and Technology Division, Los Alamos National Laboratory, Los Alamos, NM*

1. Introduction

Multicomponent Mg-Li-X-X-X alloys, where X=Al, Zn or Zr, are receiving renewed interest in many aerospace, automobile, and structural applications because of their ultra-light weight and high specific strength [1]. In addition, they have good machinability, castability, thermal conductivity, and recyclability. In comparison, the density of most commonly used Al alloys and steels is about 1.5 and 5 times larger. The hcp Mg, however, has low formability at room temperature because it has less than five independent slip systems required by the Von Mises criterion [2]. Only Basal $\langle a \rangle$ slip is activated for pure Mg at room temperature, which cannot accommodate deformation along $\langle c \rangle$ direction. A high plastic anisotropy between basal and non-basal deformation modes also impedes homogeneous deformation. Room temperature ductility and formability of Mg can be enhanced by [3]: (i) refining grain sizes by severe plastic deformation or dynamic recrystallization, (ii) modifying texture of sheet material, and (iii) adding solutes such as Li. A fundamental understanding of deformation mechanisms in simple binary NC Mg-Li alloys, which are still largely unknown, can guide us in developing stable and strong Mg-Li-X-X-X multicomponent alloys.

Figure 1 shows the large plastic anisotropy between the nucleation stresses for basal and non-basal slip modes for bulk hcp systems. Basal slip is dominant in coarse grains and a high plastic anisotropy is observed because the nucleation stress for non-basal slip is about *hundred times* higher than the basal slip. This large plastic anisotropy cannot satisfy the homogeneous deformation condition required by the Von Mises criterion, which gives rise to poor ductility and formability in bulk Mg alloys. Nanometer grain sizes [4] and alloying reduce this plastic anisotropy factor to about two, and triggers all the slip systems. In the present work, we will focus on the deformation mechanisms of Li alloying effects at the nanometer grain size in Mg.

Recently molecular dynamics (MD) was employed to reveal the deformation mechanisms in Mg NC materials [5, 6, 7, 8, 9, 10, 11, 12]. Kim et al. [5, 6] discuss the existence of basal and non-basal slip systems and twinning systems in the preferentially oriented columnar grains in the NC Mg during creep. They also studied the effect of grain size on deformation in randomly oriented 3-D NC Mg [7]. The recent paper by Moitra [8] also discusses the effect of grain size on the microstructural properties of pure Mg. Pozuelo [12] et al. investigated how twins influence deformation in Mg-Al alloys. Bhatia et al. discussed the creep behavior in Mg-Y alloys [9]. Miyazawa et al. showed the effects of segregated Al on twinning mechanisms in Mg [10]. In addition, Reddy and Groh [11] analyzed the effect of segregated Ca on the yield surfaces of NC magnesium using a MgCa-MEAM potential [13].

Our present work aims to study the strength and deformation mechanisms in randomly oriented hcp NC and single crystal Mg-Li alloys using MD simula-

[1]*Corresponding Author srinivasan.srivilliputhur@unt.edu
[2]†On leave of absence to NSF (jcaro@nsf.gov)

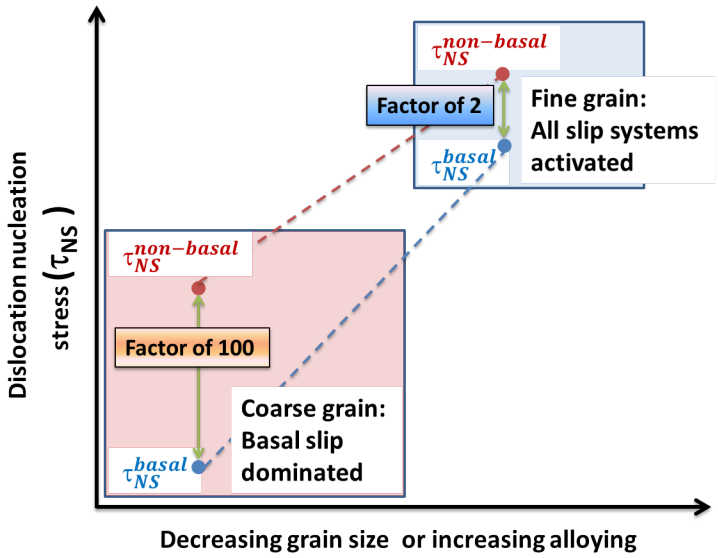

Figure 1: (Color online) A schematic diagram showing the magnitude of anisotropy in nucleation stresses of basal and non-basal slip systems (τ_{NS}) in hcp systems (adapted from [4]). The anisotropy reduces when grain size is reduced to nanoscale and/or via alloying element additions.

tions. It focuses on the qualitative and quantitative effects of Li addition in NC hcp Mg. The qualitative effects such as nucleation of deformation modes, and quantitative effects such as yield strength and formability changes are analyzed. We develop a two-parameter model that quantifies how the Li addition influences the relative ease of activating each slip system in a single crystal Mg. Nucleation stress for dislocations (τ_{NS}) and fault energy (FE) of the dislocations or twins obtained from our MD simulations are used to determine the two parameters in our model. The knowledge of the deformation processes in the single crystal Mg-Li system is then used to explain the effect of the Li addition in NC Mg.

The paper is organized as follows. Section 2 presents the simulation methodology. Section 3 reviews the slip and twin systems in hcp structure, and provides their signature in the framework of the empirical potential used in this study. Section 4 discusses the results on the mechanical behavior and deformation mechanisms in NC Mg and Mg-Li alloys. Finally, section 5 summarizes how Li addition affects individual slip systems and correlates them with deformation processes in the NC Mg-Li alloy.

2. Simulation Methodology

Large-scale Atomic/Molecular Massively Parallel Simulator (LAMMPS), a classical MD code, is used for simulations [14]. Common neighbor analysis (CNA) is used to identify the local crystal structure of atoms as face centered cubic (fcc), hcp, and to locate non-basal slip system or grain boundary atoms [15]. OVITO software is used for visualizing our simulations by highlighting crystal defects after removing thermal noise via a short minimization run [16].

A recently developed Mg-Li interatomic potential [17], based on the concentration dependent embedded atom method (CD-EAM) formalism [18], was used in this study. This potential was created from pure elemental interatomic potentials for Li and Mg [19, 20], respectively. For pure Li EAM potential, predicted values of lattice constants, cohesive energy, vacancy formation energy, melting point, and elas-

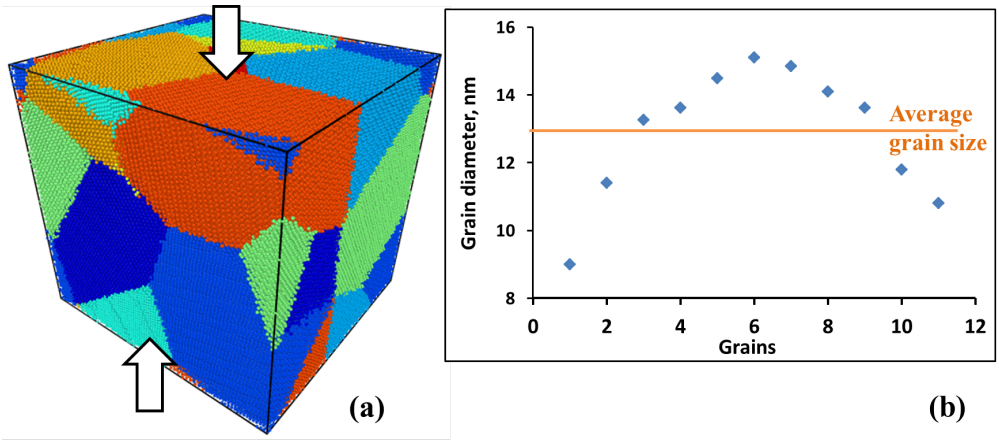

Figure 2: (Color online) (a) The nanocrystalline (NC) system, containing eleven grains, used in our simulations is shown. Atoms are colored by the identity of the grain they belong to. Arrows show the uniaxial compression direction. (b) The grain size distribution in our NC sample is shown with average grain size being 12.91nm.

tic constants are in good agreement with literature. The pure Mg EAM potential also reproduces the literature values of lattice constants, cohesive energy, melting points, and elastic constants [20]. Yasi et al. and Groh et al. [21, 22] found this potential in good agreement with first principles calculations for stacking fault energies (SFE) of basal and prismatic slip systems. Nogaret et al. and Ghazisaeidi et al. [23, 24] showed that this potential reproduces the stacking fault energy for pyramidal type I slip system but the core structure differs from density functional theory (DFT) results. They also discussed that Mg potential does not possess a stable stacking fault for the pyramidal type II slip system while *ab inito* and another Mg EAM potential [25] do. Although it was accepted that dislocation activity on the pyramidal II slip system was the main deformation mode to accommodate deformation along the $\langle c \rangle$ axis [26, 27], recent experimental analysis revealed pyramidal I as the dominant slip mode in Mg single crystal under compression along the $\langle c \rangle$ axis. The pure Mg potential used in this study describes five independent slip systems, satisfying the Von Mises criterion. Therefore, we believe that this potential can be used to model the deformation of NC magnesium. However, to validate the reliability of our CD-EAM Mg-Li potentials results, we compare the results of nucleation stresses (τ_{NS}) for different deformation modes in single crystals with recently published modified embedded atom method (MEAM) Mg-Li potential [28]. In addition, and unlike in the crystal plasticity work of Agnew et al. [29, 30], non-basal deformations resulting from Li addition can be characterized in our atomistic simulations without making prior assumptions.

The Mg-Li CD-EAM cross-potential was fitted to experimental variation of lattice constants and heat of mixing. It reproduces *composition dependent* lattice and elastic constants, heat of mixing, basal SFE, and the experimental Mg-Li phase diagram. These properties are perhaps the most relevant ones for our deformation studies. In the present paper we show an increase in the pyramidal type I SFE with Li addition, in agreement with a recent first principles study [31].

Figure 2 schematically shows the NC Mg system, containing eleven randomly oriented grains and general grain boundaries, used in our simulations. The grains are generated randomly inside the nanocrystalline (NC) simulation system. The grains are grown from randomly chosen nucleation points inside the dimensions of the NC system in random crystallographic orientations. The grains grow until they reach within a cutoff distance of 0.5Å from each

other. This construction methodology of NC system gives randomly oriented grains with general grain boundaries, which has been observed experimentally. The average diameter of each grain, calculated by multiplying the number of atoms in a grain by atomic volume, is ∼13nm. We chose this grain size to compare our results with the recent work of Moitra et al., which uses the same pure Mg potential as here [8]. They showed that nanocrystalline grains greater than 10nm diameter deform primarily via dislocation glide, whereas samples with smaller grains primarily exhibit grain boundary sliding and cracking. The grain size in the present work is therefore large enough to deform mainly by dislocation nucleation. The NC simulation cell is 231x248x234$Å^3$ and has 580964 atoms. Periodic boundary conditions are used in all directions. The NC is annealed at 300K for 100ps using the time step Δt=1fs. A Berendsen barostat is used to maintain zero external pressure, and the temperature is fixed at 300K by rescaling the velocities of the atoms. This allows the rearrangement of atoms at grain boundaries and reduces the intergranular stresses to less than 10MPa. For the Mg-Li alloys, the Li atoms replace randomly selected Mg atoms and the structure is annealed as mentioned above. We present the results for Mg-10 at.%Li system in this work. The simulation methodology for single crystals properties ($\tau_{RSS,nucl}$ and SFE) are described in the discussion section.

The NC system is uniaxially compressed in the Z direction at a strain rate of $10^8 s^{-1}$ and at 300K. Uniaxial compression along the X and Y directions also give qualitatively similar results, which suggests the population of grain boundary orientations used are large enough to address the Li addition effects on deformation mechanisms. These uniaxial compression tests allowed us to analyze the effect of Li addition in Mg on deformation mechanisms and strength variation. For Mg-Li alloys, we used three different configurations of random distributions of Li atoms for each composition. The deformation mechanisms observed in these different configurations of loading directions and Li distributions are similar, and the yield strength values are within 1% of the average values. Therefore, we only discuss results of compression along Z direction for a representative Mg-10 at.% Li system.

Mg-10 at.%Li system, predicted by our CD-EAM potential [17] as a hcp solid solution at 300K in agreement with experiments, was chosen as a reference system to study the effect of Li. We also quantify the yield strength variation as a function of Li composition and identify the underlying mechanism. Kim et al. [5, 6] observed intergranular cracking for the same EAM Mg potential [20] under tension at low plastic strains ($< 3\%$) because of the low twinning and pyramidal $\langle c+a \rangle$ slip. So, to avoid intergranular cracking, we study the deformation mechanisms under compression instead of tension. In this work, we use a NC system to sample a large diversity of stress states that display most of the unit mechanisms of plasticity in Mg-Li alloys. Therefore, we do not consider the influence of other factors such as grain size, number of grains, Li segregation at grain boundaries, and strain rate on deformation modes.

3. Slip Systems and Signatures of Deformation Modes in NC Mg and Mg-Li Alloys

Figure 3 shows the deformation modes available in the hcp metals. The available slip systems in hcp crystal structures, and the three twinning modes available to accommodate the plastic deformation along $\langle c \rangle$ direction are shown in figure 3(a) and figure 3(b), respectively. Four independent slip systems are active at room temperature – two basal slip systems on $\{0001\}$ slip plane, and two prismatic slip systems on $\{10\bar{1}0\}$ slip planes. These slip systems have Burgers vectors along $\langle a \rangle$ $\langle 11\bar{2}0 \rangle$ direction. Although the pyramidal type I and type II slip systems with Burgers vector along $\langle c+a \rangle$ $\langle 11\bar{2}3 \rangle$ are available for deformation, they are activated only at high temperature or stresses. As pyramidal I and II slip systems have high nucleation barrier at room temperature, deformation along the $\langle c \rangle$ axis is accommodated by twinning deformation at room temperature in Mg [32]. Experimentally, it was observed that addition of Li activates pyramidal slip systems at low temperatures, and increase the ductility via unknown mechanisms [29, 33].

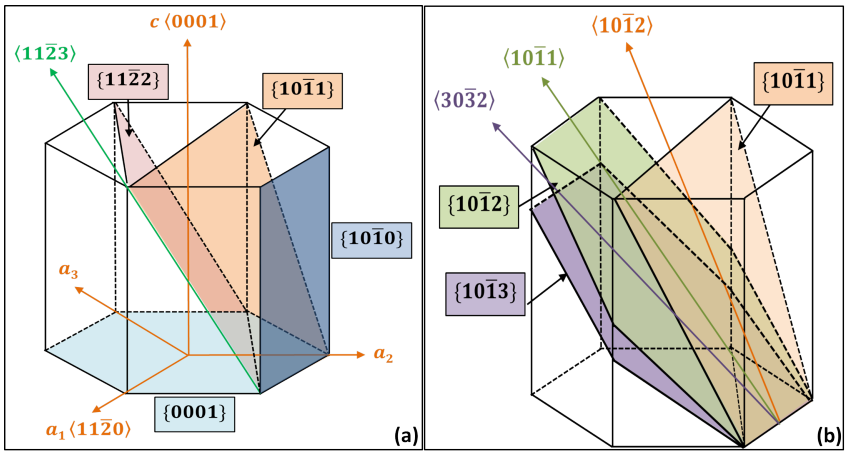

Figure 3: (Color online) Deformation modes in the hcp metals are shown. (a) Basal plane {0001} ⟨11$\bar{2}$0⟩, Prismatic plane {10$\bar{1}$0} ⟨11$\bar{2}$0⟩, Pyramidal plane type I {10$\bar{1}$1} ⟨11$\bar{2}$3⟩, and type II {11$\bar{2}$2} ⟨11$\bar{2}$3⟩ slip systems (b) tension twinning (TTW) {10$\bar{1}$2} ⟨10$\bar{1}$1⟩, compression twinning (CTW1) {10$\bar{1}$3} ⟨30$\bar{3}$2⟩, and compression twinning (CTW2) {10$\bar{1}$1} ⟨10$\bar{1}$2⟩.

Five independent deformation modes are observed in our NC compression simulations fulfilling the Von Mises criterion for homogeneous deformation. These slip systems are basal, pyramidal type I, and three twinning systems. We will summarize the signatures of individual deformation modes before discussing the complex deformation mechanisms observed in our simulations. Prismatic and pyramidal type II deformation modes are absent because they do not form a stable stacking fault for the pure Mg EAM potential and Mg-Li CD-EAM potential [17, 23], and are therefore not discussed here.

3.1. Basal dislocations

A basal dislocation dissociates into two partials via the reaction [34]:

$\frac{1}{3}[2\bar{1}\bar{1}0] = \frac{1}{3}[1\bar{1}00] + \frac{1}{3}[10\bar{1}0]$.

Figure 4 illustrates the dissociation of a $\frac{1}{3}[2\bar{1}\bar{1}0]$ dislocation in two partials with Burgers vector of type $\frac{1}{3}\langle 1\bar{1}00\rangle$ separated by a I2 (ABABCAB) stacking fault. The separation distance between the two partials is in agreement with the prediction derived from the linear elasticity.

3.2. Pyramidal type I dislocations

The dislocation core structure on the pyramidal I slip system is controversial, and, over the years, several dissociation rules were proposed [6, 35, 36, 37, 38, 39]. In this work we characterize the dislocation signature on the pyramidal type I slip system in the framework of Mg EAM potential of Sun et al. [20] using the $\{10\bar{1}1\}\ \langle 11\bar{2}3\rangle$ γ surface as reported in figure 5(a). The pyramidal I γ surface was calculated by rigidly shearing two half blocks with surface defined along the directions $\langle 1\bar{1}02\rangle$ and $\langle 11\bar{2}0\rangle$. The general shape of the pyramidal I γ surface calculated in this work is in agreement with the work of Noraget et al. [23]. As shown in figure 5(a), two stable stacking faults noted F1 and F2 are defined. Using the generalized stacking fault energy (GSFE) curve obtained for Y = 0 and Y = $\frac{1}{3}\langle 11\bar{2}0\rangle$ plotted in figure 5(b), the location of the stable stacking fault F1 and F2 are $A\langle 1\bar{1}02\rangle$ and $B\langle 1\bar{1}02\rangle + \frac{C}{3}\langle 11\bar{2}0\rangle$, respectively, with A, B, and C equal to 0.2355, 0.3469, and 1/2, respectively. Therefore, the location of the stable stacking faults F1 and F2 characterized in this work leads to a dissociation of the Burgers vector $\frac{1}{3}\langle 21\bar{1}3\rangle$ in three partials separated by two stacking faults of magnitude F1 and F2, the Burgers vectors of two of the partials being a fraction of $\langle 1\bar{1}02\rangle$. Fault F2 with lowest unstable SFE barrier to nucleate was observed in the NC simulations reported in this study whereas faults F1 was not observed due to its higher

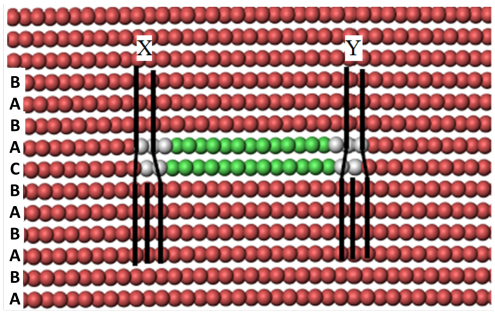

Figure 4: (Color online) A magnesium basal I2 stacking fault is shown here. Atoms are colored using CNA. Red and green atoms respectively represent the hcp and fcc atoms. The X and Y are two partials $\frac{1}{3}[1\bar{1}00]$ and $\frac{1}{3}[10\bar{1}0]$, respectively.

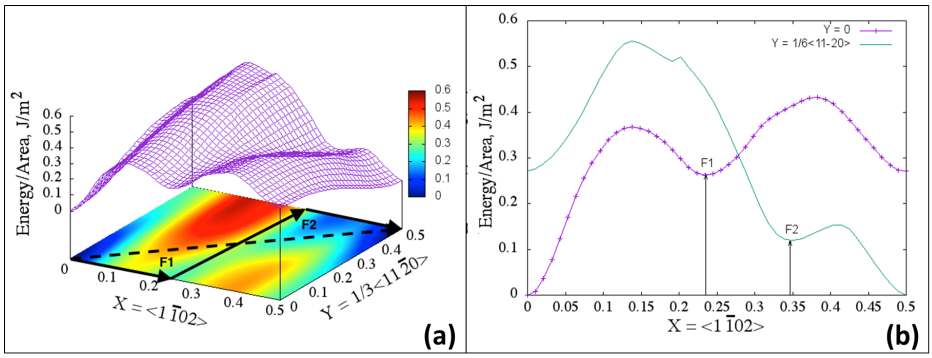

Figure 5: (Color online) (a) Stereographic and projection of the γ surface revealing the presence of two stable stacking faults F1 and F2 on the pyramidal I slip plane, and (b) GSFE curves obtained along the direction X = $\langle 1\bar{1}02\rangle$ with Y = 0 and Y = $\frac{1}{6}\langle 11\bar{2}0\rangle$. The dashed arrow represents the Burgers vector $\frac{1}{3}\langle 21\bar{1}3\rangle$, and the solid arrows represent the minimum energy path to form this Burgers vector.

nucleation barrier. The dissociation rule obtained for dislocation on the pyramidal I slip system characterized with the Mg-EAM potential is similar to the one proposed by Bacon and Liang [37] for which A, B and C are equal to $\frac{1}{4}$, $\frac{1}{3}$, and $\frac{1}{2}$, respectively.

3.3. Twins

The approach of Barrett et al. [40] is used to identify twins. First, we identify the basal plane across a twin boundary and then calculate the misorientation angle between the two mirror planes along $\langle 11\bar{2}0\rangle$ or $\langle 1\bar{1}00\rangle$ directions across the twin boundary. Figure 6 shows three twins identified in our NC simulations along with their misorientation angles. The tension twin $\{10\bar{1}2\}$ $\langle 10\bar{1}1\rangle$ is characterized by an angle of 86 degrees between parent and new grain. Whereas the two compression twins, $\{10\bar{1}3\}$ $\langle 30\bar{3}2\rangle$ and $\{10\bar{1}1\}$ $\langle 10\bar{1}2\rangle$, are characterized by a misorientation angle of 64 and 56 degrees, respectively. Hereafter we refer to tension twinning $\{10\bar{1}2\}$ as TTW, compression twinning $\{10\bar{1}3\}$ as CTW1, and compression twinning $\{10\bar{1}1\}$ as CTW2.

Table 1 summarizes various deformation modes, their abbreviations used in the text, and notations used in figures to guide the readers. Having established the signatures of important defects in the hcp systems, we now present deformation in NC Mg and Mg-Li alloy as a function of strain.

4. Deformation Mechanisms in NC Mg and Mg-Li alloys

The compressive Von Mises stress-strain plots of the NC Mg and Mg-10 at.% Li alloy at 300K are shown in figure 7. The maximum stress point on this graph is taken as the yield strength (Y). Threshold strains at which different deformation modes activate are also marked. Pure Mg yields at 0.91GPa while Mg-10 at.% Li NC yields at 0.77GPa. This decrease in the Y value with the Li addition is the so-called solid-solution softening and it occurs by changing relative activation energies of various deformation modes[3]. The interplay between the strength and ductility suggests that decrease in strength implies an increase in compressive ductility with the addition of Li. Note that our simulations did not quantify how the Li addition affects ductility of Mg alloys.

The stress-strain graphs in figure 7 show the same qualitative response for pure Mg and Mg-10 at.% Li compositions. Three distinct deformation stages are evident−(i) A linear elastic stress-strain region up to 2.75% strain. The NC sample is elastic in this region and no plastic deformation modes were evident in the bulk grains. (ii) Region with reduced hardening that extends up to 5% strain for pure Mg and 3.5% strain for Mg-10 at.% Li. Defects nucleate in this region and the yield strength point Y is observed here. (iii) Region with decreasing stress wherein twins nucleate and complex dislocation interaction processes occur.

Figure 8 shows the microstructural evolution for Mg-0 at.% Li (left) and Mg-10 at.% Li (right) at increasing strains. Microstructures are analyzed by taking multiple representative slices in the NC sample at various strains. Slices are taken at the same location for both compositions to compare deformation mechanisms. CNA is used to identify and color atoms according to their local structural environment. The hcp atoms in the bulk are colored red, fcc (green) atoms lie in basal stacking fault region, and disordered region (grey) atoms can be grain boundary, twin boundary, or pyramidal type I atoms. The capital letters represent different deformation modes – A is basal stacking fault, B pyramidal, C TTW, D CTW1, and E CTW2. These notations are also summarized in table 1. The smaller figures on the extreme right show the magnified view of the deformation mode in the regions marked by circle or ellipse. Arrows in the figure 8(e-h) show the direction of propagation of twinned regions and boundaries. Shaded areas blue, green, and yellow show the TTW, CTW1, and CTW2 twinned grain areas, respectively.

Figure 8(a-b) show stress-strain curve for the NC sample with linear elastic behavior until 2.75% strain where basal dislocations first nucleate. Once nucleated, basal dislocations are the only deformation mode present at smaller strains for both Mg-0 at.% Li and Mg-10 at.% Li. The stress-strain plot shows a non-linear behavior after this point until yield strength is achieved. The dislocation nucleation below the yield strength point is triggered by high grain boundary stresses. Basal dislocation regions

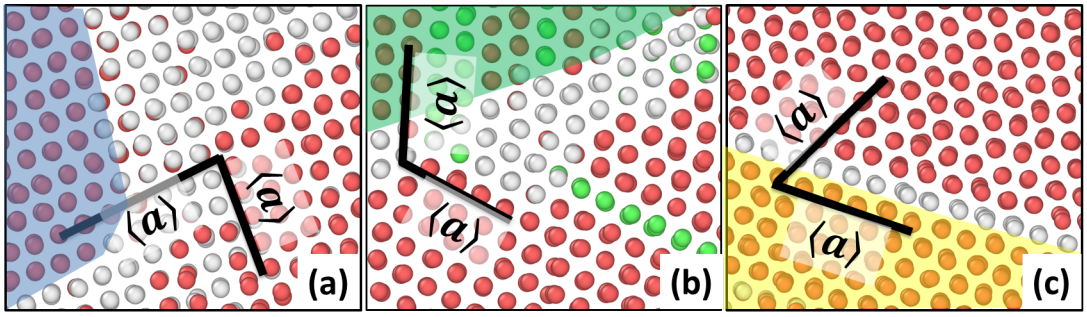

Figure 6: (Color online) Twinning systems observed in our NC Mg-Li simulations. Atoms are colored using CNA. Twin boundary atoms are colored grey color. hcp atoms in the parent and twinned grains are colored red and green atoms have fcc stacking. Black lines indicate the $\langle a \rangle$ directions in a basal plane in twinned grains. The angle between black lines are specific to the type of twin. Shaded areas show twinned grains, which are mirror images of parent grains. (a) Tension twin TTW $\{10\bar{1}2\}$ $\langle 10\bar{1}1 \rangle$ with 86^0 angle. (b) Compressive twin CTW1 $\{10\bar{1}3\}$ $\langle 30\bar{3}2 \rangle$ with 64^0 angle. (c) Compressive twin CTW2 $\{10\bar{1}1\}$ $\langle 1\bar{1}02 \rangle$ with 56^0 angle.

Table 1: Deformation modes observed in our NC simulations, and the abbreviations and notations used are summarized.

Deformation mode	Abbreviation	Plane and direction	Notation*
Basal plane	basal plane	$\{0001\}$ $\langle 11\bar{2}0 \rangle$	A
Pyramidal type I	pyramidal type I	$\{10\bar{1}1\}$ $\langle 11\bar{2}3 \rangle$	B
Tension twinning	TTW	$\{10\bar{1}2\}$ $\langle 10\bar{1}1 \rangle$	C
Compression twinning	CTW1	$\{10\bar{1}3\}$ $\langle 30\bar{3}2 \rangle$	D
Compression twinning	CTW2	$\{10\bar{1}1\}$ $\langle 10\bar{1}2 \rangle$	E

* These Notations are used in figure 8.

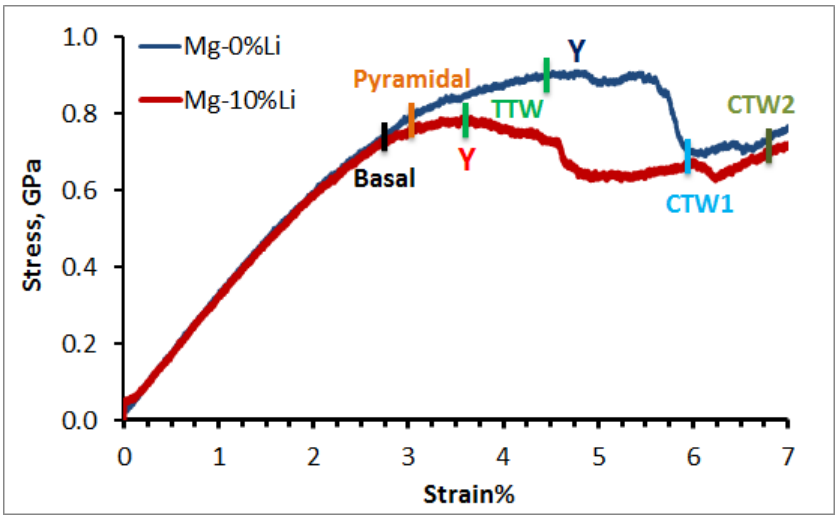

Figure 7: Compressive stress-strain response of NC Mg and Mg-10 at.% Li alloy at 300K. The yield strength (Y) decreases with Li addition in Mg. Nucleation points for various deformation modes are also marked.

circled in figure 8(a-b) are smaller for Mg-10 at.% Li compared to Mg-0 at.% Li system. Similar relative amount of basal dislocation activity is seen in the entire 3D samples for Mg-0 at.% Li and Mg-10 at.% Li. The total strain of ∼2.75% required to nucleate dislocations matches a previous study of Mg using columnar NC [5], and it is about one order of magnitude larger than the experimental values. The higher elastic strains likely result of initial defect free NC grains, high strain rates, and relatively smaller grain sizes used in MD simulations.

Figure 8(c-d) show that pyramidal type I stacking faults (B) nucleate in both compositions at 3% strain. Note the larger area of pyramidal dislocation activity in marked region of Mg-10 at.% Li system. This is also observed in the entire sample. It indicates solid solution softening for pyramidal dislocations with Li addition and lowers Von Mises stress. Thus, in the early stages of plasticity ($<$ 3%strain), basal and pyramidal type I dislocations nucleate at grain boundaries and dominate deformation processes.

Figure 8(e-f) shows that TTW nucleates at the intersection of grain boundaries and pyramidal dislocations at 3.5% and 4.75% strain for pure Mg and Mg-10 at.% Li respectively. Yield strength is reached with the nucleation of TTW, and stress drops beyond this point for both compositions. TTW activity in Mg-10 at.% Li is larger than Mg-0 at.% Li as indicated by the presence of two TTW twins in the former compared to one in the latter. In addition, TTW grows thicker in Mg-10 at.% Li at the same strain %, as shown by larger arrows and bigger shaded areas. The same trend is observed throughout the sample indicating that Li solutes promote the nucleation and propagation of TTW.

Figure 8(g-h) shows the nucleation of $\{10\bar{1}3\}$ CTW1 at 6% strain from the grain boundary of a tensile twinned (TTW) grain. Thus, TTW likely aids the nucleation of CTW1. As shown by the arrows in this figure, CTW1 propagates shorter distance in Mg-10 at.% Li. At this high strain level, basal slip and TTW activity is also pronounced. Mg-10 at.% Li shows a smaller basal stacking fault area and propagation as compared to Mg-0 at.% Li in figure 8(g-h). TTW nucleates in two grains in Mg-10 at.% Li whereas only in one grain in Mg-0 at.% Li, and a similar trend is seen in the entire NC sample.

Figure 8(i) shows that $\{10\bar{1}1\}$ CTW2 nucleates inside a grain in Mg-0 at.% Li from TTW at 6.75% strain. CTW2 activity hardens with the Li addition.

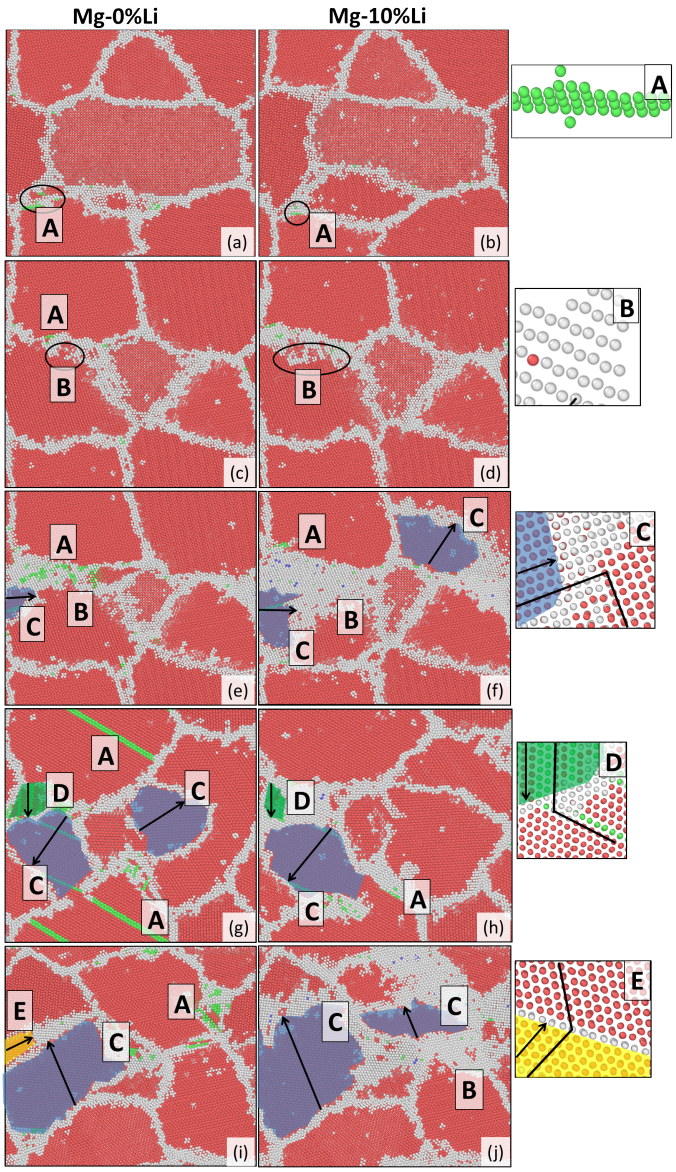

Figure 8: The deformation mechanisms in the NC Mg (left figures) and Mg-10 at.% Li (right figures) are shown as a function of increasing strains. Atoms are colored using CNA – red is hcp, green is fcc, and grey is disordered (at grain/twin boundaries and pyramidal dislocation cores). A is basal stacking fault, B pyramidal type I dislocations, C is TTW, D is CTW1, and E is CTW2. Arrow indicates the propagation direction of a twin boundary. Blue, green, and yellow shaded regions are TTW, CTW1, and CTW2 respectively. Inset shows the magnified view of the deformation mode inside marked circle or ellipses in figures in left and central columns. (a-b) At 2.75% strain: basal partials nucleate (c-d) At 3% strain: pyramidal I partials nucleate (e-f) At 4.75% strain: TTW nucleation from pyramidal type I dislocation is shown (g-h) At 6% strain: CTW1 nucleates inside grain due to tensile twinning (i-j) At 6.75% strain: CTW2 nucleates from tensile twinning.

For Mg-10 at.% Li, Figure 8(j) shows that CTW2 activity is suppressed because the TTW boundary is thicker and it propagates faster than in Mg-0 at.% Li. Less basal and more TTW activity is also seen in Mg-10 at.% Li alloys (figure 8(i-j)).

It is now clear that the presence of TTW, CTW1, and CTW2, at high strains and high plasticity regions provides additional deformation mechanisms. If we subtract the initial 2.75% elastic strain, the nucleation of TTW at low plastic strains (2.25%) from the grain boundaries, and CTW1 or CTW2 nucleation at high strains inside Mg grains or at grain boundaries matches the previous study of columnar Mg NC by Kim et al. [5] as well as some experiments [41, 42, 43, 44]. At strains greater than 5.5%, we observed some atoms in the regions of hcp, pyramidal dislocations, or twin boundaries transform to a distorted bcc phase because the hcp to bcc relative structural energy is 50% lower for the Mg potential used in this study compared to literature values [20]. Our Mg-Li CD-EAM potential calculations show that hcp-bcc transformation energy lowers by 60% when 10 at.% Li is added to Mg. These transformations occur at high strains ($> 5.5\%$) and are beyond the scope of the present work.

Now, we quantify the contribution of each deformation mode to the total plasticity by calculating the fraction of atoms in each deformation mode, the so-called relative activity R, defined as [29],

$$R = \frac{Atoms(One\ deformation\ mode)}{Atoms(All\ deformation\ modes)} \qquad (1)$$

Where the numerator is the number of atoms in an individual deformation mode such as basal, pyramidal dislocations, TTW, or CTW, and the denominator is the total number of atoms in all deformation modes. For basal stacking fault, we counted the total number of fcc atoms identified by the CNA. However, it is difficult to count the atoms in pyramidal type I slip system directly because CNA identifies pyramidal and grain boundary atoms as disordered. So the atoms in pyramidal type I slip system were manually identified by comparing the atomic structure in NC deformation simulations to that shown in figure 5(c). For twins, we first identify the hcp atoms in the twinned region based on the orientation of the initial grain and then count the number of the hcp atoms in the twinned area for the twinning mode under consideration. The comparison of R calculated at same strain values will help determine the dominant deformation mode(s) in Mg-0 at.% Li and Mg-10 at.% Li as a function of strain.

Figure 9(a-b) shows the relative activity, R, for both compositions as a function of strain. Sub-figures (a) and (b) are grouped according to hardening (basal and CTWs) or softening (pyramidal and TTW) of deformation modes with Li addition. Mg-10 at.% Li NC samples show less basal and CTW activity, and more pyramidal and TTW activity. Basal slip dominates the initial stages of plasticity in the pure Mg, while pyramidal slip accommodates most of the deformation in the Mg-10 at.% Li alloy. Thus, the easier nucleation of pyramidal dislocations as indicated by their higher activity enhances the plasticity in Mg-Li alloys and also causes the observed solid solution softening. Twinning occurs at high strains ($> 4\%$). With increase in strain, activity R of basal and pyramidal slip systems also rapidly decrease. For both the compositions, TTW becomes the major deformation mode above 4% strain. The decrease in the hardening rate after yielding coincides with TTW nucleation and growth. CTW makes negligible contribution above 6% strain. The Li addition increases TTW activity and further reduces the CTW activity.

The increase in $\langle c+a \rangle$ activity with the Li addition is consistent with previous experimental and simulation studies of Agnew et al. [29, 26, 30] and Ando et al. [45]. Other experiments have suggested a qualitative increase in $\langle c+a \rangle$ activity with Li addition [33, 26], but quantitative insights came only in year 2001 from the combined experimental and texture simulations study of Agnew et al. [29]. Here, we have successfully implemented the approach of Agnew et al. to atomistically quantify the enhancement of $\langle c+a \rangle$ pyramidal slip due to Li addition. To our best knowledge, this is the first such attempt to atomistically calculate activity and study the effect of Li addition on slip.

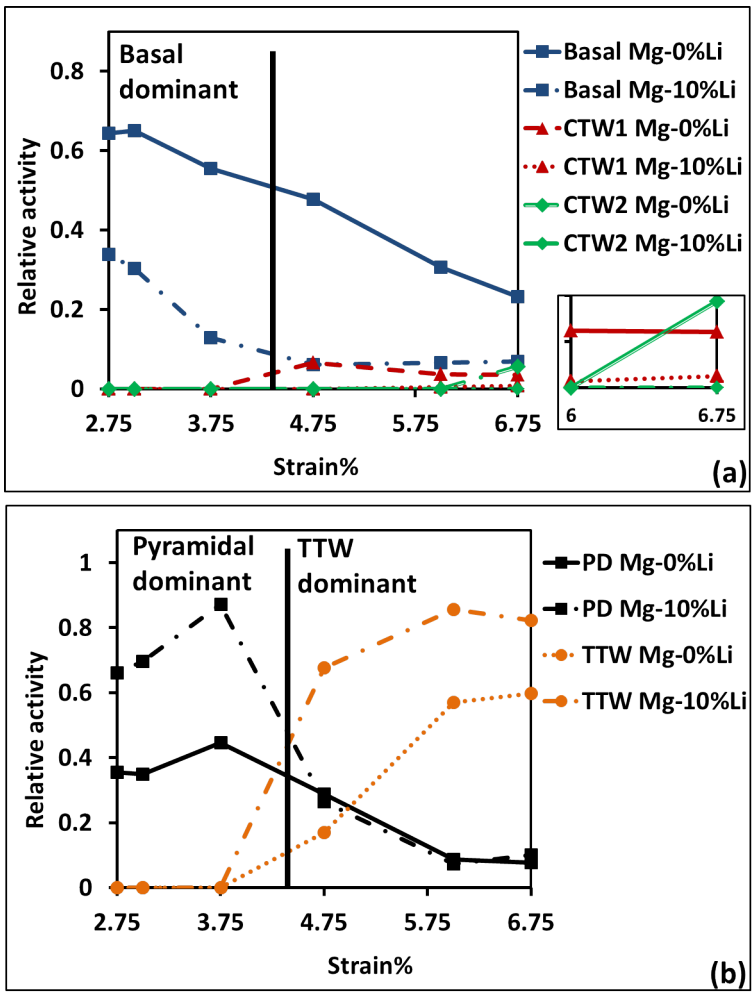

Figure 9: (Color online) The contribution of each deformation mode to total deformation (relative activity R) is plotted as a function of strain and Li addition. PD refers to pyramidal type I dislocations. The dominant deformation modes at low and high strains are demarcated by a vertical solid black line at 4.3% strain. (a) Basal and CTW1/CTW2 modes show less activity with the Li addition, which suggests that they harden. Inset shows a magnified view at high strains. (b) Pyramidal and TTW modes show increased activity suggesting softening with Li addition. Figures also show the dominant deformation mechanisms in the early stage of plasticity (basal or pyramidal) and at high plastic strains (TTW). CTW contribution at high strains is relatively small for both compositions.

5. Discussion

To understand the reduction of basal and CTW activities and the concomitant enhancement of pyramidal type I and TTW activities in Mg-Li alloys, we analyzed these deformation modes individually in Mg single crystals. We calculate the nucleation stress for dislocations (τ_{NS}) and fault energy (FE) in single crystal pure Mg and Mg-Li alloys separately for each deformation mode observed above in NC systems. Energies of stacking faults in basal and pyramidal dislocations, and twin faults in TTW, CTW1 and CTW2 are analyzed. Our goal is to understand how these parameters influence deformation behavior in pure Mg and Mg-Li NC alloys. Finally, results on the reduction in plastic anisotropy and increase in plasticity with Li addition is presented.

5.1. Unstable Stacking fault and twin fault energy (USFE and UTFE) in Mg-Li single crystals

Unstable stacking fault energy (USFE) and unstable twin fault energy (UTFE) values quantify the barriers to nucleate those two planar faults on a particular plane, their dissociation width, and stability. So, these energies provide a convenient probe to understand the effect of Li addition on atomistic deformation processes in single crystal Mg and NC Mg-Li alloys. We used the methodology of Yasi et al. [21] and Noagaret et al. [23] to calculate basal and pyramidal type I SFE respectively. For TFE calculations, we use the approach of Wang et al. and Yuasa et al. [46, 47, 48]. Ghazisaeidi et al. [49] used the same Mg potential as in this work and found that tension twin (TTW) on $\{10\bar{1}2\}$ plane is stable for 8 layer thickness lamella. We, therefore, used 8 layer twin lamella. For Mg-Li alloys, calculations are done by randomly distributing the Li atoms in simulation cell. The SFE variation for the different random distributions of Li is less than $2mJ/m^2$, so the error bars are not shown in the figures.

Figure 10(a-b) shows the SFE as a function of the Li concentration for basal and pyramidal dislocations. For pyramidal type I dislocations, only fault $F1$ is observed in the NC system (see figure 5(a)) and we discuss only its USFE here. The SFE surfaces for pure Mg match with those determined by Yasi et al. [21] for basal plane and with Nogaret et al. [23] for pyramidal type I. The USFE for basal plane increases by $\sim$40mJ/m^2 and for pyramidal type I dislocation by $\sim$20mJ/m^2 with 10 at.% Li addition. The larger increase in USFE for basal plane compared to pyramidal plane correlates well with the lower activity of basal dislocations observed in NC Mg-10 at.% Li alloys. Although the USFE for pyramidal fault increases, the increase in USFE for basal plane is twice as large as pyramidal. Therefore, the pyramidal system accommodates a larger fraction of deformation than the basal slip system in the Mg-Li alloys relative to pure Mg. Note that, basal and pyramidal slip systems are the dominant mechanisms in pure Mg and Mg-10 at.% Li alloys, respectively, below 3.75% strain as seen in figures 9(a-b). No other deformation modes are active below 3.75% strain and therefore this larger increase of USFE for basal slip as compared to pyramidal slip system plays a role in the observed activities of these slip systems. In addition, in the next sub-section 5.3, we will examine how the combined effect of basal and pyramidal USFE improves the formability of NC Mg-Li.

Figure 10(c-e) shows the TFE surfaces for TTW, CTW1, and CTW2 respectively. Point (i) shown in these figures corresponds to the stable stacking fault, which is the starting point to calculate the TFE. The layers above the stacking fault are then displaced to generate the TFE [46, 48]. The UTFE is the barrier to nucleate a stable twin fault and it occurs at point (ii). Note that a combination of shear and atomic shuffle creates twins in the hcp Mg and Mg-Li alloys. This mechanism of twin formation differs from that for fcc materials wherein twins form by pure shear [50]. As seen in figures 10(c-e), the UTFE for TTW decreases with the Li addition and increases for both types of CTW, which is consistent with the higher TTW activity and smaller CTW activity in NC Mg-Li samples. Thus, the single crystal USFE and UTFE curves satisfactorily explain the effect of Li on deformation mechanisms in NC simulations.

5.2. Nucleation stress for deformation modes in single crystals

The stress to nucleate dislocations of different types discussed earlier measures the relative ease of

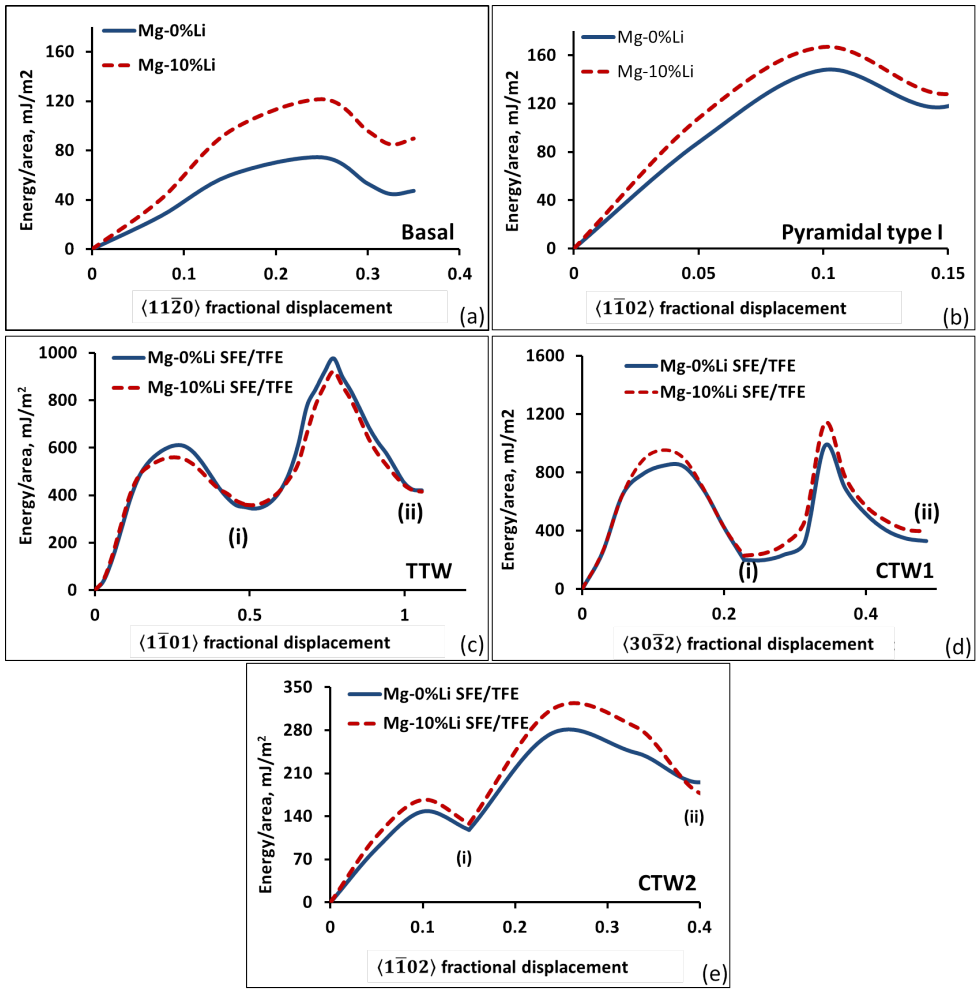

Figure 10: (Color online) SFE surfaces for (a) basal plane and (b) pyramidal dislocation type I along ⟨c⟩ ⟨1$\bar{1}$02⟩ direction are shown. (c-e) are TF energy surfaces for TTW, CTW1 and CTW2 respectively. Point (i) represents the stable SF structure for corresponding twin plane that is used as the starting point to calculate the TFE. Point (ii) represents the stable TF structure.

their nucleation. The increase in nucleation stress as a function of Li concentration indicates the presence of solid solution hardening, and vice-versa.

For each deformation mode, we chose the single crystal orientation that maximized its Schmid factor. To mimic the effect of grain boundaries present in NC simulations, we introduced lenticular cracks and free surfaces in single crystal Mg and Mg-Li alloys. This promotes heterogeneous nucleation sites for basal and pyramidal dislocations when systems are loaded under tension. The simulation system has free boundary conditions along the tensile direction and periodic boundaries along the two orthogonal directions. Lenticular cracks are not used in our twinning deformation simulations. For twins nucleation studies, free surfaces are used in all the directions, again to replicate the heterogeneous nucleation sites and grain boundary effect in NC simulations. Simulations are tensile strain controlled, with top and bottom few atomic layers held at fixed strain. To ensure consistency, we used same orientations and boundary conditions for deformations to analyze the effect of Li addition on deformation of Mg. We do not present the results for compression deformations here as the stress required to nucleate the dislocation is approximately three to four times higher than in tensile deformations and in NC simulations.

The supercell contains 20*60*60 unit cells along the X, Y and Z direction respectively. The orientations used for each deformation mode are shown in the figure 11, and tensile loading is along the Z direction. These calculations are done at 100K. Each simulation system is first annealed at 100K for 100ps using the 1fs time step to reduce the surface stress to below 5MPa. Berendsen barostat is used to control the pressure along periodic boundaries and temperature of atoms is maintained at 100K by explicitly rescaling the velocities of the atoms. For Mg-Li alloys, Li atoms are substituted at random positions and the structure is annealed at 100K. Three random distributions of Li atoms are used for Mg-Li alloys simulations and nucleation stress for each sample is within 1% of the average value.

Figure 11 plots the stress-strain curves and snapshots of the dislocation nucleation for each deformation mode. The dislocations nucleate at point N and the corresponding stress is the yield strength of a given sample. Below this point, all samples are elastic. Snapshots show various deformation modes at point N. For CTW2, full prismatic dislocations nucleate at point N because Schmid factor for prismatic dislocation is higher than CTW2. CTW2 nucleate when stress starts to drop, and the corresponding nucleation points are shown in figure 11(g). Orientation that promote nucleation of only CTW2 at yield strength point could not be established. We also do not report results for CTW1 in single crystal as we could not find an orientation that nucleates only CTW1.

Our simulations show that nucleation stress increases for basal and CTW2 mechanisms with Li addition, which means these deformation modes show solid solution hardening. This hardening is consistent with the reduced presence of these modes in Mg-Li NC materials. The nucleation stress for pyramidal type I and TTW decreases with Li addition. This suggests their increased activity in NC materials with Li addition and explains the observed softening. Yoshinaga et al. [51] observed similar qualitative trends experimentally for basal and pyramidal dislocations. They found solid solution hardening for basal planes and softening for pyramidal planes, which matches our results. Agnew et al. [29, 26] also found an increased activity of $\langle c+a \rangle$ pyramidal dislocations and decreased activity for basal dislocations with Li addition in texture simulations. Therefore, these insights on how Li affects nucleation of various deformation modes in single crystal Mg will help us understand deformation response of the NC system.

5.3. Reduction in plastic anisotropy with Li addition

Mg has poor formability because its deformation is dominated by $\langle a \rangle$ basal slip. The nucleation stress for basal and non-basal dislocations in micrometer grains differ by a factor of hundred. As stated earlier, we will investigate the effect of the solute element (Li) addition on plastic anisotropy of NC Mg. We have shown that the Li addition hardens basal and CTW modes, and softens pyramidal and TTW modes. This suggests a decrease in plastic anisotropy between basal and non-basal slip systems.

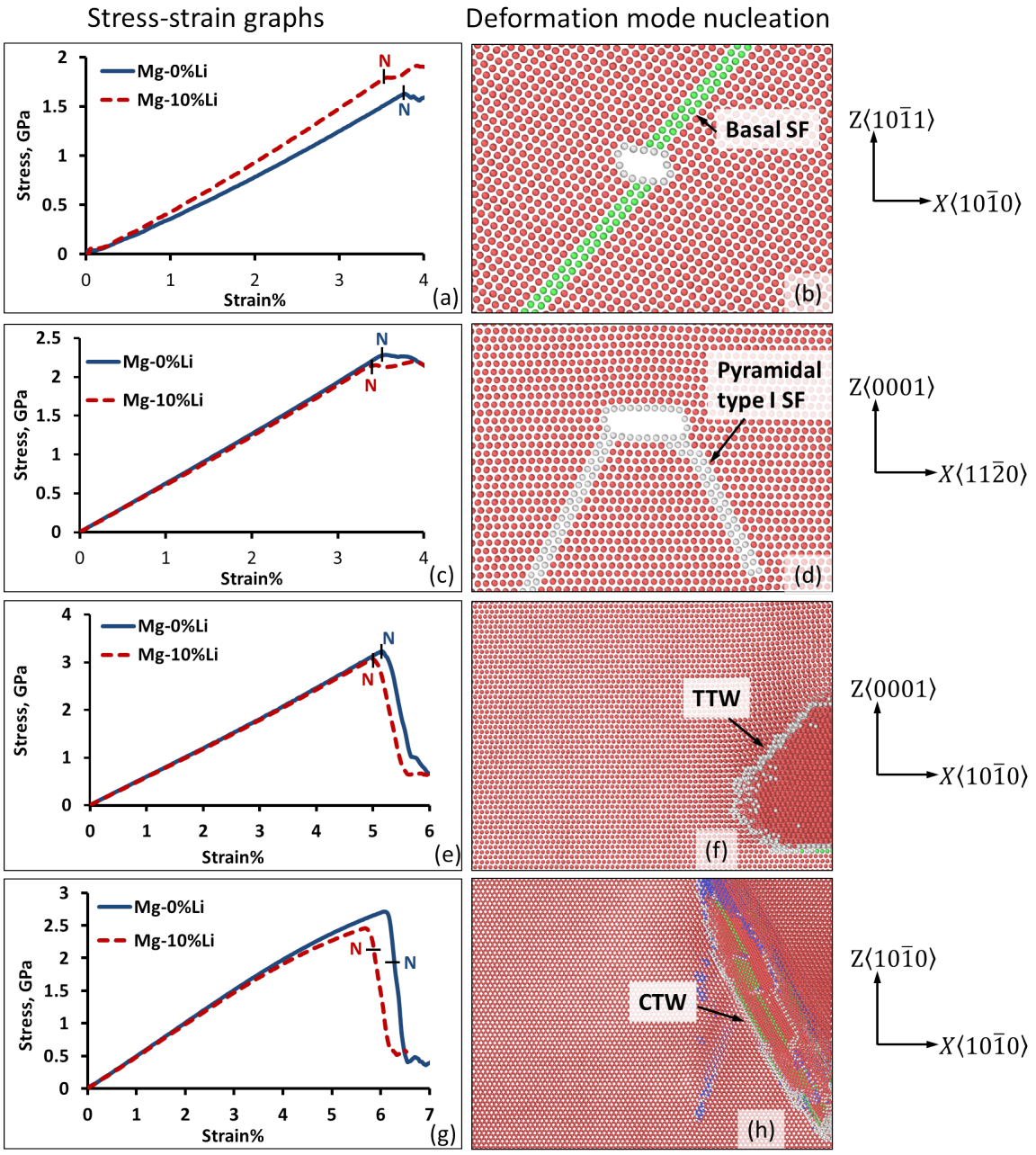

Figure 11: (Color online) Plots of Von Mises stress versus strain and the corresponding dislocation nucleation processes are shown here. N represents the dislocation nucleation points. Red atoms are hcp, green atoms lie in the basal stacking fault, blue are bcc, and grey atoms are in either disordered or in pyramidal type I stacking faults. Figures also show the corresponding microstructure at point N for basal (a-b) and pyramidal type I dislocations (c-d). The fault with disordered type atoms nucleating from cavity are pyramidal type I dislocations. Figures (e-f) and (g-h) are respectively for TTW and CTW2.

We explain this observation by correlating how resolved nucleation stress (τ_{NS}) for a particular deformation mode and unstable stacking fault energy (USFE) vary with Li addition. Figure 12 plots τ_{NS} calculated using the equation:

$$\tau_{NS} = \sigma_{nucleation} * m \tag{2}$$

Here, $\sigma_{nucleation}$ is the nucleation stress for a particular tensile deformation mode (the point N marked in figure 11) and m is the Schmid factor calculated from the orientation between the loading and slip directions. The work by Tschopp et al. [52] discusses the effect of the Schmid factor and normal factor of resolved shear stress on dislocation nucleation in fcc materials. Here we propose a plastic anisotropy criterion based on Schmid factor (see equation 2), which resolves the applied stress in the slip direction so that the nucleation stresses for different slip systems in the hcp structure can be normalized and meaningfully compared in one scale as shown in figure 12.

Pure Mg shows the lowest value of τ_{NS} for basal slip. This explains the dominance of the basal slip system in the pure Mg. The prismatic dislocations in this orientation have a slightly larger Schmid factor of 0.43 than the 0.41 value of the CTW2 system. This leads to the nucleation of prismatic dislocations before CTW2. CTW2 activity occurs only after stresses are relieved by prismatic dislocation nucleation. Note that τ_{NS} values for CTW2 should be taken only as a guidance and not as an exact value. The τ_{NS} values for pyramidal and TTW modes are higher than for basal slip. The observed differences between the τ_{NS} values for basal and non-basal slip explains the origin of factor of two in anisotropy for NC Mg.

For Mg-10 at.% Li, τ_{NS} increases for basal slip and CTW2, and decreases for pyramidal slip and TTW. This change with Li addition decreases the difference in nucleation stress between basal and non-basal modes, and reduces plastic anisotropy. It explains the dominance of pyramidal slip at low strains. Similarly, the decrease of τ_{NS} for TTW explains its higher activity at high strains.

As mentioned in the introduction, we verify the reliability of our nucleation stress τ_{NS} results for different deformation modes with a MEAM Mg-Li potential [28]. Figure 12(b) shows the τ_{NS} values from MEAM Mg-Li potential increases for basal slip system and decreases for all other non-basal deformation modes of Mg-10 at.% Li alloy. The relative decrease for the τ_{NS} values between basal and non-basal slip systems indicates a decrease in plastic anisotropy. Although the quantitative values differ slightly for CD-EAM and MEAM Mg-Li potentials, they both predict a decrease in the plastic anisotropy. The trends for individual deformation modes match qualitatively for CD-EAM and MEAM potential except for CTW2. This disagreement for CTW2 is because for CD-EAM Mg-Li potential CTW2 nucleates after prismatic dislocations are nucleated as discussed in the previous paragraph. Thus, this comparison supports our results using CD-EAM Mg-Li potential.

We quantify the reduction in plastic anisotropy with the Li addition using a plastic anisotropy parameter χ_{NS} defined as

$$\chi_{NS} = \frac{\tau_{NS}^{non-basal}}{\tau_{NS}^{basal}} \tag{3}$$

Here, $\tau_{NS}^{non-basal}$ is for the non-basal deformation mode under consideration and τ_{NS}^{basal} is the for basal dislocations. These τ_{NS} values are extracted from figure 12(a). The χ parameter is phenomenologically similar to the A parameter of by Yu et al. [4] defined as $A = \tau_{CRSS}^{non-basal}/\tau_{CRSS}^{basal}$. While the A parameter describes critical resolved shear stress for dislocation motion, the χ parameter describes the resolved nucleation stress for different deformation modes.

Table 2, shows the χ values quantifying the relative ease of nucleating different deformation modes compared to the dominant basal slip in the hcp Mg. The χ value decreases by about 25% and 33% respectively for pyramidal slip and TTW mode compared to the basal slip. This decrease shows the reduction of plastic anisotropy with Li addition in Mg-Li NC alloys.

A second empirical criterion to explain the deformation based on the unstable stacking fault energy is from Moitra et al. [31]. They define a formability parameter as the ratio of unstable stacking fault energies and given by equation 4:

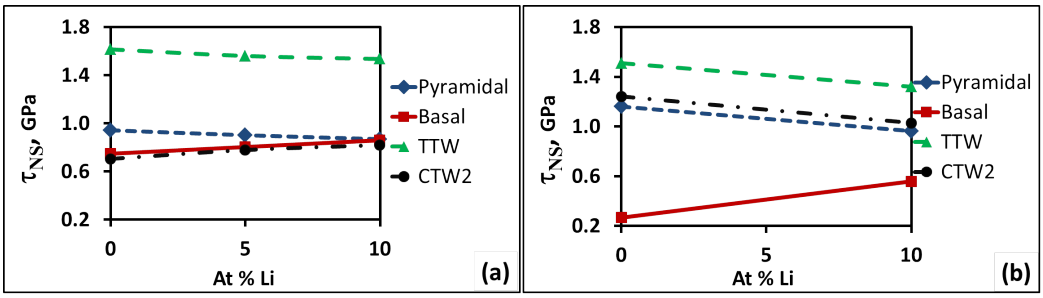

Figure 12: (Color online) Dislocation nucleation stress (τ_{NS}) for each deformation mode as a function of Li concentration is presented for (a) our CD-EAM Mg-Li potential (b) MEAM Mg-Li potential [28]. τ_{NS} is calculated using equation 2.

Table 2: The χ values for pure Mg and Mg-10 at.% Li, and their decrease with the Li addition are shown. τ_{NS} values used here are taken from figure 12.

χ (At at.% Li)	Pyramidal	TTW	CTW
χ (Mg-0 at.% Li)	1.3	2.3	1.1
χ (Mg-10 at.% Li)	1	1.5	1.1
% decrease in χ	24.2	32.9	0

$$\chi_{usf} = \frac{\frac{(\gamma^B_{usf})_X}{(\gamma^B_{usf})_{Mg}}}{\frac{(\gamma^P_{usf})_X}{(\gamma^P_{usf})_{Mg}}} \quad (4)$$

Here, γ_{usf} is unstable stacking fault energy, B and P refer to basal and pyramidal stacking faults, respectively, and X is Mg-10 at.% Li alloy concentration. The χ_{usf} parameter is calibrated by Moitra et al. for different solute additions in Mg. They found that an alloying addition increases the formability when χ_{usf} >1. This criterion takes into account the ratio of pyramidal to basal unstable stacking fault energies in the Mg-Li alloys and pure Mg. Our CD-EAM potential gives value of 1.3 for the Mg-10 at.% Li alloy and therefore is expected to increase formability. However, Moitra et al. did not explain how the ratio of unstable stacking fault energies is connected to the formability of the materials.

In this work, we propose a new formability parameter derived from physical considerations of lattice friction for dislocation motion. Note that the present work is based on the nucleation of dislocations, and the preliminary results of lattice friction are discussed. A criterion based on dislocation motion is beyond the scope of this work. As a first approximation, we consider the lattice friction given by a simple Peierls-Nabarro model in which dislocations remain planar and the generalized stacking fault energy is described by a sinusoidal function. Under these assumptions, the lattice friction is proportional to the exponential of $(-Kb/\gamma_{usf})$. Here K is the shear modulus, b is the magnitude of the Burgers vector, and γ_{usf} is the unstable stacking fault energy respectively. When written in terms of lattice friction, the formability parameter is proportional to the difference of the inverse of the unstable stacking fault energies. Therefore, the new formability parameter (F_p) is defined as:

$$F_p = K_{\langle c+a \rangle} b_{\langle c+a \rangle} \left[\frac{1}{(\gamma^P_{usf})_{Mg}} - \frac{1}{(\gamma^P_{usf})_X} \right] - K_{\langle a \rangle} b_{\langle a \rangle} \left[\frac{1}{(\gamma^B_{usf})_{Mg}} - \frac{1}{(\gamma^B_{usf})_X} \right]$$

Here, B and P are respectively the basal and pyramidal slips. The F_p value of 9.2 for CD-EAM Mg-Li potential is greater than 1. Moitra et al. [31] suggest that F_p values larger than 1 increases formability. To evaluate this criterion for these alloy systems, we used the variation of K and b for Mg-Li system from the CD-EAM Mg-Li potential and for Mg-Al system from Liu et al. [53]. These inputs yield F_p values of 17.4 and 11.3 for the two alloy systems, respectively. Because these values are greater than 1, we can argue that CD-EAM Mg-Li potential correctly predicts a qualitative increase in formability.

6. Conclusions

Our atomistic simulations systematically studied the effect of Li addition on plasticity in NC Mg-Li alloys. Li addition affects the activation of various slip systems that cause deformation. Adding 10 at.% Li reduces the plastic anisotropy by − (i) enhancing $\langle c+a \rangle$ pyramidal slip and TTW, and (ii) reducing the basal slip and CTW activity. The hardening and softening is explained using the relative activity of each mode in the NC, the fault energies, and τ_{NS} in single crystals. The Li addition decreases compressive yield strength and increases the plasticity via a higher contribution of $\langle c+a \rangle$ pyramidal and TTW activities. While basal and pyramidal type I dislocations dominate the initial stages of plasticity, twins nucleate at higher strains. The dissociation reactions for pyramidal type I dislocations are also identified for our CDEAM potential.

Single crystal parameters τ_{NS} and unstable fault energies are evaluated for each deformation mode. The stacking fault energy increases more for basal dislocations than for pyramidal type I dislocation with Li addition. TTW fault energy decreases whereas CTW1 and CTW2 fault energies increase with Li addition. Nucleation stress increases for basal slip and CTW mechanisms, and decreases for pyramidal slip and TTW mechanism. The fault energies and nucleation stress, explain the lower basal/CTW and larger pyramidal/TTW activities in Mg-Li NC samples. The τ_{NS} for different deformation modes from CD-EAM Mg-Li potential were compared against values from a MEAM Mg-Li potential [28]. Both potentials show a reduction in plastic anisotropy between basal and non-basal slip systems for pure Mg and Mg-10 at.% Li systems.

In summary, the Li addition increases the formability of NC Mg by reducing its plastic anisotropy. This is caused by the increased $\langle c+a \rangle$ pyramidal slip and TTW activity and reduced basal slip and CTW activity.

7. Acknowledgements

SVK and SGS acknowledge National Science Foundation Grant 0846444 and UNT's Talon2 computing cluster. We acknowledge useful discussions with Dr L. Capolungo (GTL, France), Dr J. Wang (LANL), Dr I. Beyerlein (LANL), Dr C. Tome (LANL), and Dr M.I. Baskes (LANL). SG aknowledges the support of the MIRACLE Project at the University of Basel founded by the Werner Siemens Foundation, Zug/Switzerland. EM gratefully acknowledges the support of the US Department of Energy (DOE) through the LANL/LDRD Program for this work.

References

References

[1] M. Avedesian, H. Baker, Magnesium and magnesium alloys, ASM specialty handbook, ASM International, 1999.

[2] G. I. Taylor, Plastic Strain in Metals, Journal of the Institute of Metals 62 (1938) 307–324.

[3] T. Al-Samman, Comparative study of the deformation behavior of hexagonal magnesium-lithium alloys and a conventional magnesium AZ31 alloy, Acta Materialia 57 (7) (2009) 2229 – 2242.

[4] Q. Yu, L. Qi, R. K. Mishra, J. Li, A. M. Minor, Reducing deformation anisotropy to achieve ultrahigh strength and ductility in Mg at the nanoscale, Proceedings of the National Academy of Sciences 110 (33) (2013) 13289–13293.

[5] D.-H. Kim, M. Manuel, F. Ebrahimi, J. Tulenko, S. Phillpot, Deformation processes in -textured nanocrystalline mg by molecular dynamics simulation, Acta Materialia 58 (19) (2010) 6217 – 6229.

[6] D.-H. Kim, F. Ebrahimi, M. Manuel, J. Tulenko, S. Phillpot, Grain-boundary activated pyramidal dislocations in nano-textured mg by molecular dynamics simulation, Materials Science and Engineering: A 528 (1617) (2011) 5411 – 5420.

[7] D.-H. Kim, Computational studies of deformation in hcp metals and defects in a lead-free ferroelectric ceramics, Ph.D. thesis, University of Florida (2011).

[8] A. Moitra, Grain size effect on microstructural properties of 3d nanocrystalline magnesium under tensile deformation, Computational Materials Science 79 (0) (2013) 247 – 251.

[9] M. A. Bhatia, S. N. Mathaudhu, K. N. Solanki, Atomic-scale investigation of creep behavior in nanocrystalline mg and mgy alloys, Acta Materialia 99 (2015) 382 – 391.

[10] M. Naoki, Y. Takashi, Y. Motohiro, C. Yasumasa, M. Mamoru, Effect of segregated al on and twinning in mg, Journal of Materials Research 30 (2015) 3629–3641.

[11] R. Reddy, S. Groh, Atomistic modeling of the effect of calcium on the yield surface of nanopolycrystalline magnesium-based alloys, Computational Materials Science 112, Part A (2016) 219 – 229.

[12] M. Pozuelo, S. Mathaudhu, S. Kim, B. Li, W. Kao, J.-M. Yang, Nanotwins in nanocrystalline MgAl alloys: an insight from high-resolution TEM and molecular dynamics simulation, Philosophical Magazine Letters 93 (11) (2013) 640–647.

[13] S. Groh, Mechanical, thermal, and physical properties of mgca compounds in the framework of the modified embedded-atom method, Journal of the Mechanical Behavior of Biomedical Materials 42 (2015) 88 – 99.

[14] S. Plimpton, Fast parallel algorithms for short-range molecular dynamics, J. of Comput. Phys. 117 (1995) 1 – 19.

[15] J. D. Honeycutt, H. C. Andersen, Molecular dynamics study of melting and freezing of small lennard-jones clusters, The Journal of Physical Chemistry 91 (19) (1987) 4950–4963.

[16] A. Stukowski, Visualization and analysis of atomistic simulation data with ovitothe open visualization tool, Modelling and Simulation in Materials Science and Engineering 18 (1) (2010) 015012.

[17] S. Karewar, N. Gupta, A. Caro, S. Srinivasan, A concentration dependent embedded atom method potential for the MgLi system, Computational Materials Science 85 (0) (2014) 172 – 178.

[18] A. Caro, D. A. Crowson, M. Caro, Classical many-body potential for concentrated alloys and the inversion of order in iron-chromium alloys, Phys. Rev. Lett. 95 (2005) 075702.

[19] P. M. Derlet, R. Hoier, R. Holmestad, K. Marthinsen, N. Ryum, The embedded-atom model applied to vacancy formation in bulk aluminium and lithium, J. Phys: Cond. Matter. 11 (1999) 3663.

[20] D. Sun, M. Mendelev, C. Becker, K. Kudin, T. Haxhimali, M. Asta, J. Hoyt, A. Karma, D. Srolovitz, Crystal-melt interfacial free energies in hcp metals: A molecular dynamics study of Mg, Phys. Rev. B 73 (2006) 1–12.

[21] J. A. Yasi, T. Nogaret, D. R. Trinkle, Y. Qi, L. G. H. Jr, W. A. Curtin, Basal and prism dislocation cores in magnesium: comparison of first-principles and embedded-atom-potential methods predictions, Model. Sim. Mater. Sci. Eng. 17 (2009) 055012.

[22] S. Groh, E. B. Marin, M. F. Horstemeyer, D. J. Bammann, Dislocation motion in magnesium: a study by molecular statics and molecular dynamics, Modelling and Simulation in Materials Science and Engineering 17 (7) (2009) 075009.

[23] T. Nogaret, W. Curtin, J. Yasi, L. H. Jr, D. Trinkle, Atomistic study of edge and screw c+a dislocations in magnesium, Acta Materialia 58 (13) (2010) 4332 – 4343.

[24] M. Ghazisaeidi, L. H. Jr, W. Curtin, First-principles core structures of edge and screw dislocations in mg, Scripta Materialia 75 (0) (2014) 42 – 45.

[25] X.-Y. Liu, J. B. Adams, F. Ercolessi, J. A. Moriarty, EAM potential for magnesium from quantum mechanical forces, Model. Sim. Mater. Sci. Eng. 4 (1996) 293.

[26] S. R. Agnew, J. A. Horton, M. H. Yoo, Metall. Mater. Trans. A 33 (2002) 851–858.

[27] E. Lilleodden, Microcompression study of mg (0001) single crystal, Scripta Materialia 62 (8) (2010) 532 – 535.

[28] Y.-M. Kim, I.-H. Jung, B.-J. Lee, Atomistic modeling of pure Li and MgLi system, Modell. Simul. Mater. Sci. Eng. 20 (2012) 035005.

[29] S. Agnew, M. Yoo, C. Tome, Application of texture simulation to understanding mechanical behavior of Mg and solid solution alloys containing Li or Y, Acta Mater. 49 (2001) 4277 – 4289.

[30] S. R. Agnew, O. Duygulu, Plastic anisotropy and the role of non-basal slip in magnesium alloy AZ31B, International Journal of Plasticity 21 (6) (2005) 1161 – 1193.

[31] A. Moitra, S.-G. Kim, M. Horstemeyer, Solute effect on the dislocation nucleation mechanism in magnesium, Acta Materialia 75 (0) (2014) 106 – 112.

[32] C. Roberts, Magnesium and its alloys, Wiley series on the science and technology of materials, Wiley, 1960.

[33] F. Hauser, P. Landon, J. Dorn, Deformation and fracture mechanisms of polycrystalline magnesium at low tempertaures, Trans. ASM 48 (1956) 986.

[34] P. G. Partridge, The crystallography and deformation modes of hexagonal close-packed metals, Metallurgical Reviews 12 (1) (1967) 169–194.

[35] B. Li, E. Ma, Pyramidal slip in magnesium: Dislocations and stacking fault on the 1011 plane, Philosophical Magazine 89 (14) (2009) 1223–1235.

[36] J. F. Stohr, J. P. Poirier, Etude en microscopie electronique du glissement pyramidal 1122 1123 dans le magnesium, Philosophical Magazine 25 (6) (1972) 1313–1329.

[37] D. J. Bacon, M. H. Liang, Computer simulation of dislocation cores in h.c.p. metals i. interatomic potentials and stacking-fault stability, Philosophical Magazine A 53 (2) (1986) 163–179.

[38] M. H. Liang, D. J. Bacon, Computer simulation of dislocation cores in h.c.p. metals ii. core structure in unstressed crystals, Philosophical Magazine A 53 (2) (1986) 181–204.

[39] S. Ando, H. Tonda, T. Gotoh, Molecular dynamics simulation of c+a dislocation core structure in hexagonal-close-packed metals, Metallurgical and Materials Transactions A 33 (3) (2002) 823–829.

[40] C. Barrett, H. E. Kadiri, M. Tschopp, Breakdown of the schmid law in homogeneous and heterogeneous nucleation events of slip and twinning in magnesium, Journal of the Mechanics and Physics of Solids 60 (12) (2012) 2084 – 2099.

[41] D. Brown, S. Agnew, M. Bourke, T. Holden, S. Vogel, C. Tome, Internal strain and texture evolution during deformation twinning in magnesium, Materials Science and Engineering: A 399 (12) (2005) 1 – 12.

[42] J. Koike, Enhanced deformation mechanisms by anisotropic plasticity in polycrystalline Mg alloys at room temperature, Metallurgical and

Materials Transactions A 36 (7) (2005) 1689–1696.

[43] X. Lou, M. Li, R. Boger, S. Agnew, R. Wagoner, Hardening evolution of AZ31B Mg sheet, International Journal of Plasticity 23 (1) (2007) 44 – 86.

[44] M. Lentz, R. Coelho, B. Camin, C. Fahrenson, N. Schaefer, S. Selve, T. Link, I. Beyerlein, W. Reimers, In-situ, ex-situ EBSD and HR-TEM analyses of primary, secondary and tertiary twin development in an Mg 4 wt percent Li alloy, Materials Science and Engineering: A 610 (0) (2014) 54 – 64.

[45] S. Ando, H. Tonda, Non-basal slip in magnesium-lithium alloy single crystals, Materials Transactions, JIM 41 (9) (2001) 1188–1191.

[46] J. Wang, J. Hirth, C. Tome, Twinning nucleation mechanisms in hexagonal-close-packed crystals, Acta Materialia 57 (18) (2009) 5521 – 5530.

[47] J. Wang, R. Hoagland, J. Hirth, L. Capolungo, I. Beyerlein, C. Tome, Nucleation of a twin in hexagonal close-packed crystals, Scripta Materialia 61 (9) (2009) 903 – 906.

[48] M. Yuasa, M. Hayashi, M. Mabuchi, Y. Chino, Atomic simulations of $(10\bar{1}2)$,$(10\bar{1}1)$ twinning and $(10\bar{1}2)$ detwinning in magnesium, Journal of Physics: Condensed Matter 26 (1) (2014) 015003.

[49] M. Ghazisaeidi, W. A. Curtin, Analysis of dissociation of c and c + a dislocations to nucleate 10-12 twins in mg, Modelling and Simulation in Materials Science and Engineering 21 (5) (2013) 055007.

[50] H. V. Swygenhoven, P. M. Derlet, A. G. Frseth, Stacking fault energies and slip in nanocrystalline metals, nature materials 3 (2004) 399–403.

[51] H. Yoshinaga, R. Horiuchi, On the flow stress of alpha solid solution Mg-Li alloy single crystals, Transactions of the Japan Institute of Metals 4 (3) (1963) 134–141.

[52] M. A. Tschopp, D. L. McDowell, Tension-compression asymmetry in homogeneous dislocation nucleation in single crystal copper, Applied Physics Letters 90 (12) (2007) 121916.

[53] X.-Y. Liu, J. Adams, Grain-boundary segregation in Al-10%Mg alloys at hot working temperatures, Acta Materialia 46 (10) (1998) 3467 – 3476.